High-performance integrated perovskite and organic solar cells with efficient near-infrared harvesting

Junghwan Kim[a], Kwanghee Lee[a,b]*

[a]Department of Electrical and Computer Engineering, University of Toronto, 10 King's College Road, Toronto, Ontario, Canada, M5S 3G4
[b]School of Materials Science and Engineering, Gwangju Institute of Science and Technology, Gwangju 61005, Republic of Korea
E-mail: K. Lee (klee@gist.ac.kr)

ABSTRACT

The integration of planar-type perovskite ($E_g \sim 1.5$ eV) solar cells (PSCs) with a bulk-heterojunction (BHJ) composite comprising a near-infrared (NIR) absorbing conjugated polymer ($E_g < 1.4$ eV) and a fullerene derivative is a promising approach to overcoming the narrow absorption limit of typical PSCs. Nevertheless, integrated solar cells (ISCs) suffer from low fill factors (FFs) and inefficient NIR harvesting, mainly due to poor charge transport in the BHJ films. Here, we successfully demonstrate highly efficient P-I-N perovskite/BHJ ISCs with an enhanced FF and improved NIR harvesting by introducing a novel n-type semiconducting polymer and a new processing additive into the BHJ films. The optimized ISCs exhibit a power conversion efficiency (PCE) of 16.36%, which far surpasses that of the reference PSCs ($\sim$ 14.70%) due to the increased current density ($J_{sc} \sim 20.04$ mA cm^{-2}) resulting from the additional NIR harvesting. Meanwhile, the optimized ISCs maintain a high FF of 77% and an open-circuit voltage (V_{oc}) of 1.06 V. These results indicate that this approach is a versatile means of overcoming the absorption and theoretical efficiency limits of state-of-the-art PSCs.

Keywords: Perovskite solar cell; Organic solar cell; Integrated solar cell; Fill factor; NIR harvesting

1. INTRODUCTION

Due to the intensive researches on the development of high-quality perovskite films,[1-3] new device architectures,[4-7] and compositional engineering[8-10] as well as a fundamental understanding of the charge dynamics[11,12] and the device operational mechanisms,[13][14][15] there have been tremendous progresses in the field of perovskite solar cells (PSCs) and power conversion efficiencies (PCEs) of over 20% have been reported for the PSCs.[16] However, most state-of-the-art efficient PSCs based on methylammonium lead iodide (MAPbI$_3$) or formamidinium lead iodide (FAPbI$_3$) only utilize solar radiation below a wavelength of $\sim$ 800 nm, leaving the majority of the near-infrared (NIR) range unused.[8,11] Therefore, if PSC researchers are able to find a way to utilize NIR solar radiation efficiently, it is possible to further improve the PCE to values approaching the Shockley–Queisser limit.[17]

One promising approach to broadening the absorption range of PSCs above 800 nm is to integrate perovskite and a bulk-heterojunction (BHJ) as an interlayer-free, parallel-like tandem cell, a so-called 'integrated' perovskite/organic solar cell (ISC).[18,19] In general, the BHJ in ISCs is a photoactive layer composed of an NIR absorbing conjugated polymer (or small molecule) and a fullerene derivative typically used in organic solar cells (OSCs). Because both films (perovskite and BHJ) have ambipolar charge transporting properties, the electrons and holes generated in both films can be collected at each electrode, as in two-terminal parallel tandem devices. Therefore, by combining a perovskite as a UV-vis absorber and a BHJ layer as an NIR absorber in ISCs, it is possible to harvest full-range light, covering the UV to NIR solar spectrum (Fig. 1a). Moreover, in contrast to conventional series/parallel tandem devices, ISCs can be easily fabricated by monolithically stacking perovskite and BHJ without interlayers because of their mutual solvent orthogonality. Furthermore, ISCs do not suffer from thermalization losses originating from the current and/or voltage mismatch among subcells, as encountered in conventional series and parallel tandem cells.[20,21]

Unfortunately, there have been only two reports which studied on the ISC devices until now, and the device performances of the ISCs are relatively lower than those of typical PSCs.[18,19] Especially, their low fill factors (FFs), which are far below the typical values (~ 80%) of conventional PSCs, and inefficient NIR harvesting hinder further enhancement of the ISC performance. Although there is a large room to further improve the PCE of the ISCs, it is still unclear what a crucial factor is for designing and realizing high performance ISCs.

In this work, we have investigated the effects of BHJ morphology on P-I-N type ISCs combining a MAPbI$_3$ perovskite and an NIR absorbing organic BHJ, revealing a crucial design rule for high efficiency of the ISCs. The BHJ, composed of diketopyrrolopyrrole (DPP)-based low bandgap polymer (LBP) DT-PDPP2T-TT (TT) and [6,6]-phenyl C$_{71}$ butyric acid methyl ester (PC$_{71}$BM), was elaborately adjusted by introducing a novel n-type polymer, poly{[N,N'-bis(2-octyldodecyl)-naphthalene-1,4,5,8-bis(dicarboximide)-2,6-diyl]-alt-5,5'-(2,2'-bithiophene)}, P(NDI2OD-T2) (also known as N2200) as an electron transport enhancer and diphenyl ether (DPE) as a solvent processing additive. The optimized perovskite/BHJ ISC devices with well-distributed bicontinuous BHJ networks and a high electron mobility of 10^{-2} cm^2 V^{-1} s^{-1} exhibit a dramatically increased current density (17.61 mA cm^{-2} to 20.04 mA cm^{-2}) due to the additional NIR harvesting, while maintaining the high FF (77%) and V$_{oc}$ (1.06 V) characteristic of typical PSCs. The resulting PCE is 16.36%, which is the highest value for the reported ISC systems and far surpasses the 14.70% value achieved using the reference PSCs without any BHJ layer.

2. EXPERIMENTAL METHODS

2.1 Materials

All materials, including PbI$_2$, reagents, and solvents, were purchased from Sigma-Aldrich unless otherwise stated. The low bandgap polymer TT, the n-type semiconducting polymer N2200, and PC$_{71}$BM were purchased from One Materials, Polyera, and Nano-C, respectively, and were used as received. The CH$_3$NH$_3$I was synthesized by reacting 27.86 mL methylamine (40% in methanol) and 30 mL hydroiodic acid (57 wt%) in a 250 mL round-bottomed flask at 0 °C for 2 h with stirring. A yellowish raw product (CH$_3$NH$_3$I) was obtained using a rotary evaporator and was re-dissolved in 80 mL absolute ethanol; a white-coloured powder (CH$_3$NH$_3$I) was formed via the addition of 300 mL ethyl acetate. After filtration, the powder was washed repeatedly with ethyl acetate. Recrystallization from ethanol yielded a pure crystal of CH$_3$NH$_3$I. The crystal was collected and dried at 60 °C in a vacuum oven for 24 h. A 1.5 M solution of MAPb(I$_{1-x}$Br$_x$)$_3$ (x = 0.1) was prepared by dissolution of PbI$_2$, PbBr$_2$, and CH$_3$NH$_3$I powders in γ-butyrolactone:DMSO (dimethyl sulfoxide) mixed solvent (7:3, volume ratio) at 60 °C for 1 day. For the soluble VO$_x$ precursor solution, vanadium-oxytri-isopropoxide ((C$_3$H$_7$O)$_3$VO) was dissolved in isopropyl alcohol (IPA) at a 1:300 volume ratio. The n-doped TiO$_x$ solution was synthesized according to a previous method.[22]

2.2 Fabrication of planar-heterojunction perovskite solar cells

Patterned ITO/glass substrates (15 Ω/sq) were cleaned with detergent, ultrasonicated in acetone and isopropyl alcohol, and subsequently dried overnight in an oven. For the hole transport layer of the PHJ single perovskite and perovskite/BHJ solar cells, PEDOT:PSS (AI 4083) solution was spin-cast in air onto the pre-cleaned and UV/ozone-treated ITO/glass substrate at 5,000 rpm for 30 s (~ 25 nm thickness). The films were then annealed on a hot plate at 150 °C for 10 min, and VO$_x$ solution (1:300 in IPA) was spin-cast in air onto the PEDOT:PSS followed by treatment at 150 °C for 10 min. The substrate (ITO/PEDOT:PSS/VO$_x$) was transferred into a N$_2$-filled glove box, where 1.5 M MAPb(I$_{1-x}$Br$_x$)$_3$ (x = 0.1) solution was coated onto the ITO/PEDOT:PSS/VO$_x$ substrate by two consecutive spin-coating steps at 800 rpm and 4,000 rpm for 20 s and 60 s, respectively. During the second spin-coating step, 600 μL toluene was quickly dripped onto the rotating substrate. After drying the substrate at 100 °C for 10 min, the transparent film was completely converted into a dark-brown perovskite film. For the single PSCs, PC$_{61}$BM solution (40 mg/ml in CB) was deposited onto the perovskite film. In the case of perovskite/BHJ integrated solar cells, solutions of BHJ (TT:PC$_{71}$BM = 4 mg:12 mg/ml) processed from CB or CB:DPE (97:3, volume ratio) solvents were spin-cast by controlling the rotating speed to optimize the film thickness. To further increase the electron transport, 1 mg of N2200 was introduced into the BHJ processed from CB:DPE. After drying the BHJ films, n-doped TiO$_x$ film was deposited onto the BHJ films. Finally, Al was thermally evaporated on top of the devices through a shadow mask (4.64 mm^2) at ~ 1 x 10^{-6} Torr.

2.3 Characterization of the planar-heterojunction perovskite solar cells

The *J-V* characteristics were measured using a Keithley 237 source measure unit in an N_2 atmosphere. The solar-cell parameters were obtained using an AM 1.5 G solar simulator with an irradiation intensity of 100 mW·cm^{-2}. The lamp was calibrated with an NREL-calibrated KG5 filtered silicon reference cell. The IPCE measurements were conducted using a QEX10 solar cell instrument (PV Measurement, Inc., USA) with a chopping frequency of 100 Hz. The surface morphology of the films was measured by AFM (Park Systems Corp., XE-100). The SEM measurements were conducted using an S-4700 SEM instrument (Hitachi, Japan). Steady-state PL spectra were obtained with a F-7000 fluorescence spectrometer (Hitachi, Japan) by photoexciting the samples at 470 nm. Time-resolved PL measurements were conducted using a timecorrelated single photon counting (TCSPC) setup (PicoQuant, Germany) with a 470 nm picosecond pulsed laser source (PicoQuant, LDH-P-C-470) and laser drivers (PicoQuant, PDL 800-D). The PL was collected at a wavelength of 760 nm using an imaging triple grating monochromator/spectrograph (Princeton Instruments, Acton SP2300, USA).

3. RESULTS AND DISCUSSION

Figure 1a presents the schematic device architecture of the ISC combining the NIR absorbing BHJ and the UV-vis absorbing perovskite layer. The ISCs were constructed based on a P-I-N planar type architecture with a structure of ITO/poly(3,4-ethylenedioxythiophene) polystyrene sulfonate (PEDOT:PSS)/soluble vanadium oxide (VO_x)/perovskite/BHJ/n-doped TiO_x/Al, where the PEDOT:PSS/VO_x layers act as hole transport/collection layers. Based on the ITO/PEDOT:PSS/VO_x anode substrate, a uniform perovskite film, $MAPb(I_{1-x}Br_x)_3$ (x = 0.1), was formed with high crystallinity using the two-step solvent dripping method reported by Seok et al (Fig. 1c).[2] On top of the perovskite film, the BHJ, comprising an LBP of TT as a donor and $PC_{71}BM$ and N2200 as acceptors, was introduced as an NIR harvesting layer. The role of N2200 will be described in detail later in this work. The chemical structures and absorption spectra of the materials used in the BHJ film are shown in Figure 1b and 1d, respectively. The LBP of TT absorbs NIR radiation up to 920 nm above the absorption edge of the perovskite. To further optimize our P-I-N-integrated solar cells, a nitrogen (N)-doped TiO_x layer was adopted the BHJ film to enhance the electron selectivity and reduce the contact resistance between the BHJ and Al electrode.[22,23]
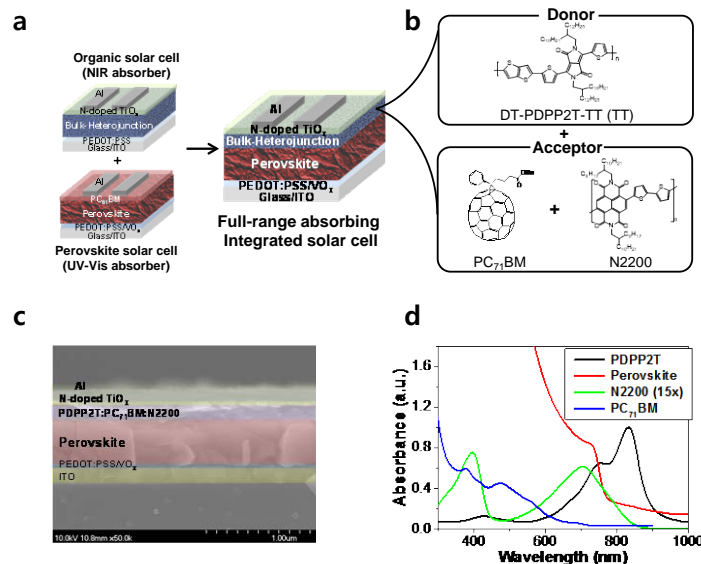

Figure 1. (a) Device architecture of the P-I-N type integrated solar cell obtained from organic and perovskite solar cells. (b) Chemical structures of the organic donor and acceptor materials: DT-PDPP2T-TT, $PC_{71}BM$, and N2200. (c) Cross-sectional SEM image of the integrated device. (d) Absorption spectra of the component materials.

To investigate the effects of the BHJ morphology on device performance, we prepared three BHJ films: conventional binary-blended BHJ processed from chlorobenzene (CB) solvent, BHJ processed from mixed solvent of CB:DPE (97:3

vol%), and N2200-included BHJ processed from mixed CB:DPE (97:3 vol%) solvent. Figure 2a-c present the defocused bright-field transmission electron microscopy (TEM) images of the three BHJ films (CB, CB:DPE, and CB:DPE:N2200). Based on the different electron densities, the bright and dark regions are designated as TT polymer/N2200 and $PC_{71}BM$, respectively. For the conventional binary BHJ film (CB), there is a large-scale phase separation between the TT and $PC_{71}BM$. The TT polymer shows interconnected bundle-like aggregations, whereas the $PC_{71}BM$ molecules form disconnected agglomerates with a size of ~ 100 nm, hindering the efficient exciton diffusion/dissociation and electron transport (Figure 2a). However, as shown in Figure 2b, the binary BHJ film processed from CB:DPE shows a dramatically improved morphology with well distributed bicontinuous networks of TT and $PC_{71}BM$, implying efficient charge transport. This observation indicates that the addition of small amounts of the processing additive DPE enhances the miscibility of the two organic materials and facilitates the formation of intimate contacts.[24] Similar features are also observed in the N2200-included BHJ (CB:DPE:N2200) film. One distinctive feature is that the N2200-included films show a more pronounced fibril structure, which is attributed to the higher content of the n-type polymer N2200 in the BHJ.

The surface roughness and topology of the BHJ films were also investigated by atomic force microscopy (AFM). As shown in Figure 2d-f, the BHJ films from CB:DPE and CB:CPELN2200 exhibit smooth surfaces with root-mean-square (RMS) roughnesses of 1.5 nm and 1.2 nm, respectively, whereas the film from CB has a relatively uneven surface, with an RMS roughness of 2.7 nm.
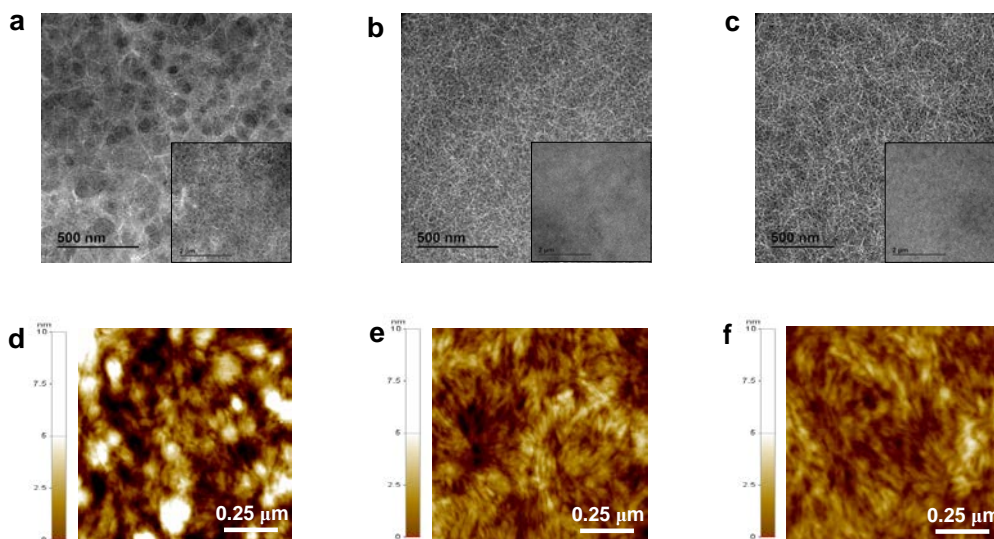

Figure 2. TEM and AFM images of BHJ films processed from CB (a, d), CB:DPE (b, e), and CB:DPE:N2200 (c, f), respectively.

Based on the structural analysis of the BHJ films, we characterized the optical and electrical properties of the BHJ films. As shown in Figure 3a, the optical absorption measurements showed that the three BHJ films have similar absorptivities of ~ 10^4 cm^{-1} regardless of film morphology, indicating that the light absorption of the BHJ films does not critically depend on the BHJ morphology. However, the charge transport behaviour is strongly influenced by the BHJ morphology.[25,26]
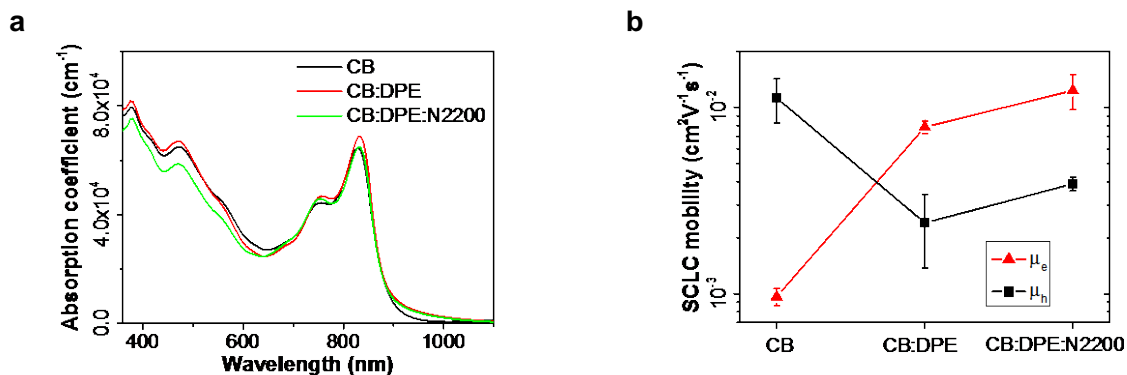
Figure 3. Absorption coefficient spectra (g) and SCLC electron- and hole-mobility (h) of the BHJ layers with CB, CB:DPE, and CB:DPE:N2200.

Figure 3b shows the electron (μ_e) and hole (μ_h) mobilities of the three BHJ films in the vertical direction extracted from the space charge limited current (SCLC) measurement.[27] The electron mobility of the binary BHJ processed from CB is significantly enhanced, from μ_e ~9.6 x 10^{-4} cm^2 V^{-1} s^{-1} to μ_e ~7.8 x 10^{-3} cm^2 V^{-1} s^{-1}, by the addition of DPE, and it is further increased to μ_e ~1.2 x 10^{-2} cm^2 V^{-1} s^{-1} after adding DPE:N2200. Regarding the hole mobility, the binary BHJ from CB has μ_h ~1.1 x 10^{-2} cm^2 V^{-1} s^{-1}, which decreases to μ_h ~2.4 x 10^{-3} cm^2 V^{-1} s^{-1} and μ_h ~3.9 x 10^{-3} cm^2 V^{-1} s^{-1} for DPE and DPE:N2200 processed BHJ, respectively. Based on the charge balance (= μ_h/μ_e), the CB:DPE-BHJ and CB:DPE:N2200-BHJ films exhibit better charge-balancing values (0.3 and 0.32, respectively) than the CB-BHJ films (~ 11.6), which is beneficial for device performance. Bearing in mind the results of the TEM measurements, the charge transport behaviour is consistent with the morphology changes of the BHJ films induced by the introduction of the DPE and N2200; the morphology change from the large-scale phase separation with large disconnected $PC_{71}BM$ agglomerates and interconnected bundle-like TT aggregation in the CB-BHJ films to the well-distributed bicontinuous networks between the TT and $PC_{71}BM$/N2200 for the CB:DPE:N2200-BHJ films. More importantly, we found that adding a small amount of the high-mobility n-type polymer N2200 into the binary BHJ further increases the electron mobility of the BHJ, indicating that N2200 facilitates the formation of percolation pathways for electron transport.
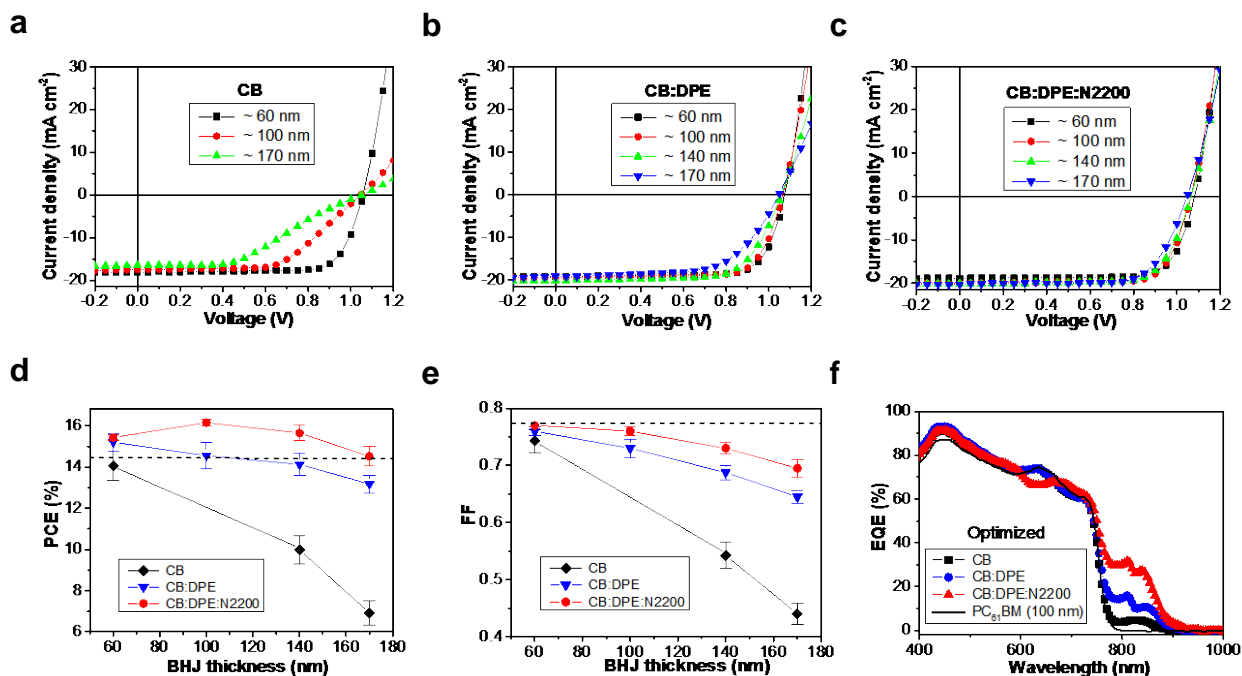

Figure 4. J-V curves of integrated solar cells with various BHJ film thicknesses processed from CB (a), CB:DPE (b), and CB:DPE:N2200 (c). The plots of the PCE (d) and FF (e) for the integrated solar cells as a function of the BHJ film thickness. The dotted lines are guided for those of optimized control PSC. EQE spectra (f) of the optimized control PSC (PC61BM) and integrated solar cells incorporating CB, CB:DPE, and CB:DPE:N2200 processed BHJ films.

To explore the effects of the BHJ morphology on the device performance, we fabricated perovskite/BHJ ISCs with a device architecture of ITO/PEDOT:PSS/VO$_x$/perovskite (~ 350 nm)/BHJ/n-doped TiO$_x$/Al, where the BHJ films were processed from CB, CB:DPE, and CB:DPE:N2200. Figure 4a-c shows the *J-V* characteristics of the ISCs incorporating various BHJ thicknesses and the detailed characteristics are included in Table 1. To demonstrate the effects of the BHJ morphology and film thickness on device performance, the PCE and FF values of the ISCs were plotted as a function of BHJ film thickness (see Fig. 4d and e). The dotted lines indicate the corresponding values (PCE = 14.70%, J_{sc} = 17.61 mA cm^{-2}, V_{oc} = 1.07 V, and FF = 78%) of the optimized control PSC (ITO/PEDOT:PSS/VO$_x$/perovskite/PC$_{61}$BM/Al) in our work. As shown in Fig. 4d, for the ISCs with BHJ from CB and CB:DPE, the device performance was optimized by incorporating 60-nm-thick BHJ layers. As the thickness of the binary BHJ layers (CB and CB:DPE) increased from 60 nm to 170 nm, the FF values decreased monotonously, in contrast to the increase in J_{sc} resulting from additional NIR harvesting, causing a degradation of the overall efficiencies. For the integrated solar cells with ternary blend BHJ (CB:DPE:N2200), however, the FFs exhibit high values (above 72%) despite the increase in the BHJ thickness to 170 nm, and the highest efficiency was achieved with 100 nm-thick BHJ film due to a dramatically enhanced J$_{sc}$ and a high FF. As a result, the ISCs with the CB:DPE:N2200-BHJ film present the highest efficiency, 16.36%, with J_{sc} ~ 20.04 mA cm^{-2}, V_{oc} ~ 1.06 V, and FF ~ 77%. In comparison, the efficiencies of the other integrated devices with CB-BHJ and CB:DPE-BHJ are 14.50% and 15.72%, respectively. Especially, the PCE of the reference PSC was dramatically improved from 14.70% to 16.36% due to the increased J_{sc} (17.61 mA cm^{-2} → 20.04 mA cm^{-2}) resulting from the introduction of the BHJ processed from CB:DPE:N2200. These results are in agreement with the trend of the SCLC electron mobilities of the BHJ films, indicating that high electron mobility is a key parameter for efficient P-I-N type ISCs. In particular, the integrated device with CB:DPE:N2200-BHJ films presents higher efficiency and FF than the CB-BHJ and CB:DPE-BHJ integrated devices, indicating that the synergetic effects of DPE and N2200 played a crucial role in high-performance ISCs.

These behaviours can be explained by the EQE spectra of the devices, which are shown in Figure 4f. As observed in Figure 4f, unlike the control PSC, the perovskite/BHJ ISCs exhibit additional light harvesting in the NIR region (800 nm ~ 920 nm) above the absorption edge of the perovskite. Comparing the enhanced EQE (ΔEQE = EQE$_{BHJ}$ − EQE$_{PC61BM}$) with the absorption spectrum of the low bandgap TT polymer, it is clear that the integration of PSCs with NIR absorbing BHJs is an effective strategy for extending the absorption bandwidth of the perovskites, thereby further improving the efficiency of PSCs. More importantly, because our optimized BHJ layers effectively provide additional light harvesting in the NIR without sacrificing other key parameters of the PSCs, such as the high V$_{oc}$ and FF, enhanced efficiencies exceeding 20% are expected to be attained upon the integration of more efficient film formation techniques for MAPbI$_3$ or FAPbI$_3$ perovskites with our optimized BHJ layers.
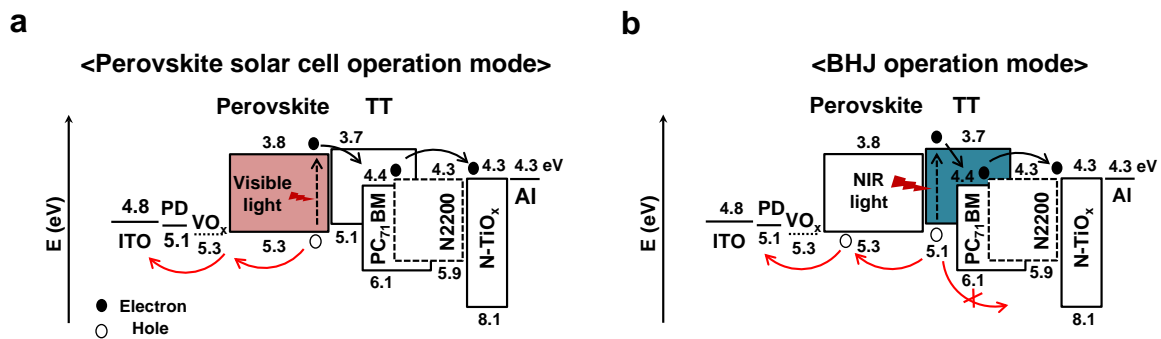

Figure 5. Energy level diagrams of the integrated device for perovskite operation mode (a) and BHJ operation mode (b).

From the correlation between the BHJ morphology and device performance of the ISCs, the low performance of the previously reported ISCs seems to originate from the poor charge transport and short exciton diffusion length (L_D) of the organic components in the non-optimized BHJ films. Figure 5 presents the two operation modes ('perovskite operation mode' and 'BHJ operation mode') of the ISC. In the perovskite operation mode (Figure 5a), the perovskite layer absorbs

the majority of the UV-vis solar radiation and generates excitons, which can be easily dissociated into free holes and electrons at the interfaces of VO_x/perovskite and perovskite/$PC_{71}BM$, respectively, due to their low exciton binding energy (E_{bi}). In the BHJ operation mode, however, the low bandgap polymer of TT mainly absorbs the NIR radiation and generates tightly bound excitons (Fig. 1d). To efficiently dissociate the excitons into free charges, it is crucial to form intimate contact between the conjugated polymer and the fullerene derivative within the distance of L_D ($\sim$ 20 nm) for typical conjugated polymers.[25,28] In addition, considering the excellent charge transport property and L_D of the perovskites, for high-performance P-I-N type ISCs, the free electrons generated in both films (perovskite and BHJ) should travel efficiently through the BHJ to be collected at the top Al electrode. Therefore, it is concluded that the optimization of the BHJ resulting in a high electron mobility and intimate donor polymer and acceptor molecule contacts is a crucial factor maximizing the performance of the ISCs.

4. CONCLUSIONS

In conclusion, we have successfully demonstrated highly efficient P-I-N type perovskite/BHJ ISCs with enhanced FF and high NIR harvesting by optimizing the BHJ morphology. The BHJ, comprising a low bandgap polymer of TT and $PC_{71}BM$, was optimized by introducing both a DPE solvent and N2200, a high-mobility n-type polymer, resulting in the formation of well-distributed bicontinuous network for efficient charge transfer/transport as well as the enhancement of the electron mobility up to 10^{-2} cm^2 V^{-1} s^{-1}. From the correlation between the BHJ morphology and device performance of the integrated devices, we found that the formation of an intimate BHJ morphology with high electron transport plays a vital role for the P-I-N type perovskite/BHJ ISCs to exhibit efficient light harvesting from the UV to NIR, as well as high FF and V_{oc} values. Consequently, we have significantly enhanced the PCE of the control PSC from 14.70% to 16.36% by increasing J_{sc} via the additional NIR harvesting while maintaining a high FF (77%) and V_{oc} (1.06 V). To the best of our knowledge, this PCE is by far the highest efficiency for reported ISCs. This work proves the feasibility of highly efficient ISCs with panchromatic absorption as a new photovoltaic architecture and provides important design rules for optimizing ISCs.

Table 1. Device performance parameters of single PSCs and perovskite/BHJ integrated solar cells.

		V_{oc} (V)	J_{sc} (mA cm^{-2})	FF	PCE (%) (best)
Perovskite/PC$_{61}$BM		1.07	17.64 ± 0.07	0.77 ± 0.08	14.50 ± 0.18 (**14.70**)
Perovskite/BHJ (CB)	60 nm	1.05 ± 0.004	18.00 ± 0.38	0.74 ± 0.02	14.07 ± 0.71 (**14.85**)
	140 nm	1.05 ± 0.004	17.50 ± 0.72	0.54 ± 0.02	9.99 ± 0.67 (**10.64**)
	170 nm	1.05 ± 0.005	15.04 ± 1.04	0.44 ± 0.02	6.92 ± 0.58 (**7.43**)
Perovskite/BHJ (CB:DPE)	60 nm	1.07 ± 0.005	18.79 ± 0.28	0.76 ± 0.007	15.21 ± 0.42 (**15.72**)
	100 nm	1.06 ± 0.009	18.89 ± 0.33	0.73 ± 0.02	14.55 ± 0.65 (**15.53**)
	140 nm	1.05 ± 0.007	19.71 ± 0.27	0.69 ± 0.01	14.24 ± 0.53 (**14.90**)
	170 nm	1.04 ± 0.008	19.69 ± 0.36	0.65 ± 0.01	13.18 ± 0.42 (**13.77**)
Perovskite/BHJ (CB:DPE:N2200)	60 nm	1.07 ± 0.004	18.69 ± 0.11	0.77	15.43 ± 0.15 (**15.31**)
	100 nm	1.06 ± 0.004	20.08 ± 0.08	0.76 ± 0.01	16.16 ± 0.16

		V_{oc} (V)	J_{sc} (mA cm^{-2})	FF	PCE (%) (best)
					(16.36)
	140 nm	1.06 ± 0.005	20.32 ± 0.13	0.73 ± 0.01	15.65 ± 0.38 **(16.08)**
	170 nm	1.05 ± 0.005	19.99 ± 0.18	0.70 ± 0.02	14.52 ± 0.48 **(15.31)**

(Reverse scan at 20 msec delay time, average PCE derived from 10 samples)

ACKNOWLEDGEMENTS

REFERENCES

[1]   Burschka, J., Pellet, N., Moon, S.-J., Humphry-Baker, R., Gao, P., Nazeeruddin, M. K.., Gratzel, M., "Sequential deposition as a route to high-performance perovskite-sensitized solar cells," Nature **499**(7458), 316–319 (2013).

[2]   Jeon, N. J., Noh, J. H., Kim, Y. C., Yang, W. S., Ryu, S.., Seok, S. Il., "Solvent engineering for high-performance inorganic–organic hybrid perovskite solar cells," Nat. Mater. **13**(9), 897–903 (2014).

[3]   Liu, M., Johnston, M. B.., Snaith, H. J., "Efficient planar heterojunction perovskite solar cells by vapour deposition," Nature **501**(7467), 395–398 (2013).

[4]   Lee, M. M., Teuscher, J., Miyasaka, T., Murakami, T. N.., Snaith, H. J., "Efficient Hybrid Solar Cells Based on Meso-Superstructured Organometal Halide Perovskites," Science **338**(6107), 643–647 (2012).

[5]   Heo, J. H., Im, S. H., Noh, J. H., Mandal, T. N., Lim, C.-S., Chang, J. A., Lee, Y. H., Kim, H., Sarkar, A., et al., "Efficient inorganic-organic hybrid heterojunction solar cells containing perovskite compound and polymeric hole conductors," Nat Phot. **7**(6), 486–491 (2013).

[6]   Liu, C., Wang, K., Du, P., Yi, C., Meng, T.., Gong, X., "Efficient Solution-Processed Bulk Heterojunction Perovskite Hybrid Solar Cells," Adv. Energy Mater. **5**(12), 14022024(1-7) (2015).

[7]   Wang, K., Liu, C., Du, P., Zheng, J.., Gong, X., "Bulk heterojunction perovskite hybrid solar cells with large fill factor," Energy Environ. Sci. **8**(4), 1245–1255 (2015).

[8]   Eperon, G. E., Stranks, S. D., Menelaou, C., Johnston, M. B., Herz, L. M.., Snaith, H. J., "Formamidinium lead trihalide: a broadly tunable perovskite for efficient planar heterojunction solar cells," Energy Environ. Sci. **7**(3), 982–988 (2014).

[9]   Lee, J.-W., Seol, D.-J., Cho, A.-N.., Park, N.-G., "High-Efficiency Perovskite Solar Cells Based on the Black Polymorph of HC(NH2)2PbI3," Adv. Mater. **26**(29), 4991–4998 (2014).

[10]   Jeon, N. J., Noh, J. H., Yang, W. S., Kim, Y. C., Ryu, S., Seo, J.., Seok, S. Il., "Compositional engineering of perovskite materials for high-performance solar cells," Nature **517**(7535), 476–480 (2015).

[11]   Stranks, S. D., Eperon, G. E., Grancini, G., Menelaou, C., Alcocer, M. J. P., Leijtens, T., Herz, L. M., Petrozza, A.., Snaith, H. J., "Electron-Hole Diffusion Lengths Exceeding 1 Micrometer in an Organometal Trihalide Perovskite Absorber," Science **342**(6156), 341–344 (2013).

[12]   Xing, G., Mathews, N., Sun, S., Lim, S. S., Lam, Y. M., Grätzel, M., Mhaisalkar, S.., Sum, T. C., "Long-Range Balanced Electron- and Hole-Transport Lengths in Organic-Inorganic CH3NH3PbI3," Science **342**(6156), 344–347 (2013).

[13]   Lin, Q., Armin, A., Nagiri, R. C. R., Burn, P. L.., Meredith, P., "Electro-optics of perovskite solar cells," Nat Phot. **9**(2), 106–112 (2015).

[14] Ponseca, C. S., Savenije, T. J., Abdellah, M., Zheng, K., Yartsev, A., Pascher, T., Harlang, T., Chabera, P., Pullerits, T., et al., "Organometal Halide Perovskite Solar Cell Materials Rationalized: Ultrafast Charge Generation, High and Microsecond-Long Balanced Mobilities, and Slow Recombination," J. Am. Chem. Soc. **136**(14), 5189–5192 (2014).

[15] Xu, J., Buin, A., Ip, A. H., Li, W., Voznyy, O., Comin, R., Yuan, M., Jeon, S., Ning, Z., et al., "Perovskite-fullerene hybrid materials suppress hysteresis in planar diodes," Nat Commun **6,** 7081(1-8) (2015).

[16] Yang, W. S., Noh, J. H., Jeon, N. J., Kim, Y. C., Ryu, S., Seo, J.., Seok, S. Il., "High-performance photovoltaic perovskite layers fabricated through intramolecular exchange," Science **348**(6240), 1234–1237 (2015).

[17] Nayak, P. K.., Cahen, D., "Updated Assessment of Possibilities and Limits for Solar Cells," Adv. Mater. **26**(10), 1622–1628 (2014).

[18] Zuo, C.., Ding, L., "Bulk heterojunctions push the photoresponse of perovskite solar cells to 970 nm," J. Mater. Chem. A **3**(17), 9063–9066 (2015).

[19] Liu, Y., Hong, Z., Chen, Q., Chang, W., Zhou, H., Song, T.-B., Young, E., Yang, Y., You, J., et al., "Integrated Perovskite/Bulk-Heterojunction toward Efficient Solar Cells," Nano Lett. **15**(1), 662–668 (2015).

[20] Bailie, C. D., Christoforo, M. G., Mailoa, J. P., Bowring, A. R., Unger, E. L., Nguyen, W. H., Burschka, J., Pellet, N., Lee, J. Z., et al., "Semi-transparent perovskite solar cells for tandems with silicon and CIGS," Energy Environ. Sci. **8**(3), 956–963 (2015).

[21] You, J., Dou, L., Hong, Z., Li, G.., Yang, Y., "Recent trends in polymer tandem solar cells research," Prog. Polym. Sci. **38**(12), 1909–1928 (2013).

[22] Kim, G., Kong, J., Kim, J., Kang, H., Back, H., Kim, H.., Lee, K., "Overcoming the Light-Soaking Problem in Inverted Polymer Solar Cells by Introducing a Heavily Doped Titanium Sub-Oxide Functional Layer," Adv. Energy Mater. **5**(3), 1401298(1-5) (2015).

[23] Kim, J. Y., Kim, S. H., Lee, H. H., Lee, K., Ma, W., Gong, X.., Heeger, A. J., "New Architecture for High-Efficiency Polymer Photovoltaic Cells Using Solution-Based Titanium Oxide as an Optical Spacer," Adv. Mater. **18**(5), 572–576 (2006).

[24] Choi, H., Ko, S.-J., Kim, T., Morin, P.-O., Walker, B., Lee, B. H., Leclerc, M., Kim, J. Y.., Heeger, A. J., "Small-Bandgap Polymer Solar Cells with Unprecedented Short-Circuit Current Density and High Fill Factor," Adv. Mater. **27**(21), 3318–3324 (2015).

[25] Li, G., Zhu, R.., Yang, Y., "Polymer solar cells," Journal Article, Nat Phot. **6**(3), 153–161 (2012).

[26] Guo, X., Zhou, N., Lou, S. J., Smith, J., Tice, D. B., Hennek, J. W., Ortiz, R. P., Navarrete, J. T. L., Li, S., et al., "Polymer solar cells with enhanced fill factors," Nat Phot. **7**(10), 825–833 (2013).

[27] Blom, P. W. M., de Jong, M. J. M.., van Munster, M. G., "Electric-field and temperature dependence of the hole mobility in poly(p-phenylene vinylene)," Phys. Rev. B **55**(2), 656–659 (1997).

[28] Kong, J., Hwang, I.-W.., Lee, K., "Top-Down Approach for Nanophase Reconstruction in Bulk Heterojunction Solar Cells," Adv. Mater. **26**(36), 6275–6283 (2014).